

# Auxetics-Inspired Tunable Metamaterials for Magnetic Resonance Imaging

Ke Wu, Xiaoguang Zhao, Thomas G. Bifano, Stephan W. Anderson,\* and Xin Zhang\*

Auxetics refers to structures or materials with a negative Poisson's ratio, thereby capable of exhibiting counterintuitive behaviors. Herein, auxetic structures are exploited to design mechanically tunable metamaterials in both planar and hemispherical configurations operating at megahertz (MHz) frequencies, optimized for their application to magnetic resonance imaging (MRI). Specially, the reported tunable metamaterials are composed of arrays of interjointed unit cells featuring metallic helices, enabling auxetic patterns with a negative Poisson's ratio. The deployable deformation of the metamaterials yields an added degree of freedom with respect to frequency tunability through the resultant modification of the electromagnetic interactions between unit cells. The metamaterials are fabricated using 3D printing technology and an  $\approx 20$  MHz frequency shift of the resonance mode is enabled during deformation. Experimental validation is performed in a clinical (3.0 T) MRI system, demonstrating that the metamaterials enable a marked boost in radiofrequency field strength under resonance-matched conditions, ultimately yielding a dramatic increase in the signal-to-noise ratio ( $\approx 4.5\times$ ) of MRI. The tunable metamaterials presented herein offer a novel pathway toward the practical utilization of metamaterials in MRI, as well as a range of other emerging applications.

metamaterial antennas,<sup>[7]</sup> among others. In terms of the application of metamaterials in magnetic resonance imaging (MRI), magnetic metamaterials composed of an array of unit cells featuring metallic wires or helices have been utilized to enhance the signal-to-noise ratio (SNR) of MRI by amplifying the RF magnetic field strength.<sup>[8,9]</sup> In order to achieve optimal performance, a frequency matched condition between the metamaterials and the MRI systems must be ensured. However, as metamaterials are susceptible to differences in patient body composition, their resonance frequency may shift to undesired higher or lower values when in proximity to patients of varying body composition. Another notable limitation of many conventional metamaterials reported to date for enhancing SNR in MRI systems is their planar distribution of unit cells, which is limited in imaging curved surfaces, such as the brain, breast, or musculoskeletal system (knee, ankle, etc.). As the SNR gains of metamaterials decrease as a function of distance from

## 1. Introduction

Efforts in developing metamaterials have progressed from initial demonstrations of breaking the generalized limitations of refraction and reflection of natural materials, to their current use in facilitating a range of practical applications, such as super lenses,<sup>[1,2]</sup> perfect absorbers,<sup>[3,4]</sup> cloaking devices,<sup>[5,6]</sup> and


the metamaterial surface, ensuring a conformal approximation between the metamaterial and the surface of the object of interest is crucial to optimizing performance.

Metamaterials incorporating active materials or those featuring variable impedance within or as part of the metamaterial elements have been reported to exhibit tunable electromagnetic (EM) properties, which are modulated by external influences or signals, such as optical excitation,<sup>[10]</sup> thermal heating,<sup>[11]</sup> or biased voltage.<sup>[12]</sup> Physical perturbation of the structure, by moving subsets of the unit cells fabricated on stretchable substrates<sup>[13]</sup> or using microelectromechanical systems (MEMS) devices to adjust the orientation or relative location of a fraction of the unit cells,<sup>[14]</sup> has also been employed to yield the capacity for EM tunability. However, with respect to metamaterials for MRI applications, the focus herein, operating an additional optical or thermal source to modulate the resonance frequency is challenging given the unique environment of MRI. Furthermore, while it is possible to achieve an EM tunability by inserting variable capacitors or varactors, the requisite additional electrical circuitry to control this system would yield an appreciable increase in complexity and cost. In the case of magnetic metamaterials, one of the most straightforward approaches to realize tunability is to adjust the separation distance between unit cells. The effect of interunit cell

K. Wu, X. Zhao, X. Zhang  
Department of Mechanical Engineering  
Boston University  
Boston, MA 02215, USA  
E-mail: xinz@bu.edu

K. Wu, X. Zhao, T. G. Bifano, S. W. Anderson, X. Zhang  
Photonics Center  
Boston University  
Boston, MA 02215, USA  
E-mail: sande@bu.edu

X. Zhao, S. W. Anderson  
Department of Radiology  
Boston University Medical Campus  
Boston, MA 02118, USA

 The ORCID identification number(s) for the author(s) of this article can be found under <https://doi.org/10.1002/adma.202109032>.

DOI: 10.1002/adma.202109032

distance on near field coupling has been both theoretically and experimentally investigated, from microwave to terahertz frequencies.<sup>[15,16]</sup> However, manual geometric tuning by adjusting the interunit cell distance is precluded given the centimeter-scale of the unit cells and the millimeter-scale of the desired uniform physical perturbations required for frequency tuning. Therefore, we developed a novel method to realize tunability by employing a type of mechanical metamaterial, namely, auxetic cellular structures.

Auxetics refers to 2D or 3D materials and structures that preserve their global shape during expansion and contraction.<sup>[17–20]</sup> Their geometries exhibit a counter-intuitive deformation under uniaxial compression (tension) and transverse contraction (expansion), which is characterized by a negative Poisson's ratio  $\nu$ . These mechanical properties offer auxetics broad application, including advanced textiles,<sup>[21]</sup> tunable filters,<sup>[22]</sup> hierarchical stents,<sup>[23]</sup> piezoelectric devices,<sup>[24]</sup> and vibration dampers,<sup>[25]</sup> to name a few. Since the auxetic effect results from their particular internal cellular structure, structures of arbitrary geometry from 2D to 3D may be further tailored by using variable cell geometry and well-defined topologies. Furthermore, an advantage that auxetic tuning schemes possess is scalability and adaptability, properties that support the increasingly common use of these technologies. Relevant to the work presented herein, the unique properties of auxetics provide a pathway toward realizing tunable 2D and 3D metamaterials for MRI applications. Here, we employ auxetic patterns to construct tunable 2D and 3D magnetic metamaterials composed of arrays of unit cells featuring metallic helices, capable of resonance frequency tuning for MRI. A resonance frequency tuning range ( $\approx 20$  MHz) is achieved using a mechanically actuated scaffold frame to adjust the relative position between unit cells in a uniform manner, thereby modulating the coupling between neighboring unit cells. The capacity for tuning yielded an optimized frequency match between the metamaterial and the MRI system, thereby maximizing the degree of increase in RF strength and, ultimately, the SNR of the resultant images.

## 2. Results

### 2.1. 2D Tunable Metamaterial

With respect to the design of 2D tunable metamaterials for use in MRI, the unit cells should be arranged uniformly such that a uniform magnetic field distribution in the vicinity of the metamaterial is achieved. In addition, the constituent materials of the unit cells should be readily available in conventional 3D printing technology as this greatly eases design and process modification, thereby decreasing lead-time from concept to prototype. Considering these requirements, the rotating polygonal model, a classic type of auxetic structure, is adopted in the case of the 2D tunable MRI metamaterial presented herein. The auxeticity of the rotating polygonal model results from the arrangement of rigid polygons connected together at their vertices by hinges,<sup>[26]</sup> with the deformation mechanism shown in **Figure 1a**. Upon application of an external load, the rigid polygons rotate with respect to one another, with the horizontal and vertical separation distances between neighboring unit cells

simultaneously contracting or expanding and giving rise to a negative Poisson's ratio  $\nu$ , which may be expressed by<sup>[19]</sup>

$$\nu_{21} = (\nu_{21})^{-1} = \frac{a^2 \sin^2\left(\frac{\theta}{2}\right) - b^2 \cos^2\left(\frac{\theta}{2}\right)}{a^2 \cos^2\left(\frac{\theta}{2}\right) - b^2 \sin^2\left(\frac{\theta}{2}\right)} \quad (1)$$

where the geometric parameters  $a$ ,  $b$ , and  $\theta$  are defined in **Figure 1a**. In order to yield a uniform distribution and degree of contraction or expansion in the horizontal and vertical directions for the metamaterial, here we set  $a = b$ , which gives rise to a negative Poisson's ratio of  $-1$ . Considering the configuration of magnetic metamaterials in MRI,<sup>[9]</sup> we employed an inner circle surrounded by four linkages to replace the polygon in the auxetic model, as shown in **Figure 1a**. As a proof of concept of the tunable metamaterial, cylindrical plastic scaffolds were 3D printed featuring grooves along their upper, outer surface, and used to define the shape of the helical metallic coils, including the space between turns and the number of turns. Following printing, copper wire was wound into the scaffolding grooves to form the metallic resonator composing each unit cell of the metamaterial array. In addition, at the lower, outer surface of the scaffolding, female or male supports were employed such that these unit cells could subsequently be connected by pins to form larger arrays of unit cells, with the hinge joints allowing for rotation of the unit cells, thereby giving rise to the auxetic effect; see **Figure 1b**. In this 2D tunable metamaterial design, the outer and inner diameters of the cylinder were 30 and 23 mm, respectively, and the length of male and female supports were both 3.5 mm. As a result, the separation distance  $Dis$  between individual unit cells could be varied within the range from 30 to 37 mm. **Figure 1c** illustrates the deformation process, demonstrating the auxetic nature of the metamaterial featuring a negative Poisson's ratio. The fabrication results may be found in **Section S1** and **Figure S1** in the Supporting Information.

The working principle of MRI metamaterials lies in the coupling of the helical metallic coils composing the individual unit cells. The synergy of these helical coils gives rises to a resonance mode in which the direction of the electric current induced by an applied RF field is identical in each coil. When excited by the external RF field transmitted from the MRI during RF transmission, the induced currents in the resonant mode lead to a dramatic enhancement of the RF field. When the frequency of the resonant mode closely approximates the working frequency of the MRI system, marked gains in both local transmit and receive RF magnetic fields are achieved, ultimately leading to enhancement in the SNR of the resultant images.<sup>[9]</sup> As above, the mechanical properties resulting from the auxetic nature of the metamaterial array allow for an adjustable separation distance  $Dis$  for the array. However, more directly relevant are the effects on the electromagnetic properties of the metamaterial when applied to MRI. Thus, we turn to analyses of the influence of the metamaterial's configuration on its electromagnetic properties, namely, the modulation of its resonance frequency and the variation of the magnetic field enhancement in the vicinity of the metamaterial. We consider the operating frequency (127 MHz) of the 3 T clinical MRI system employed

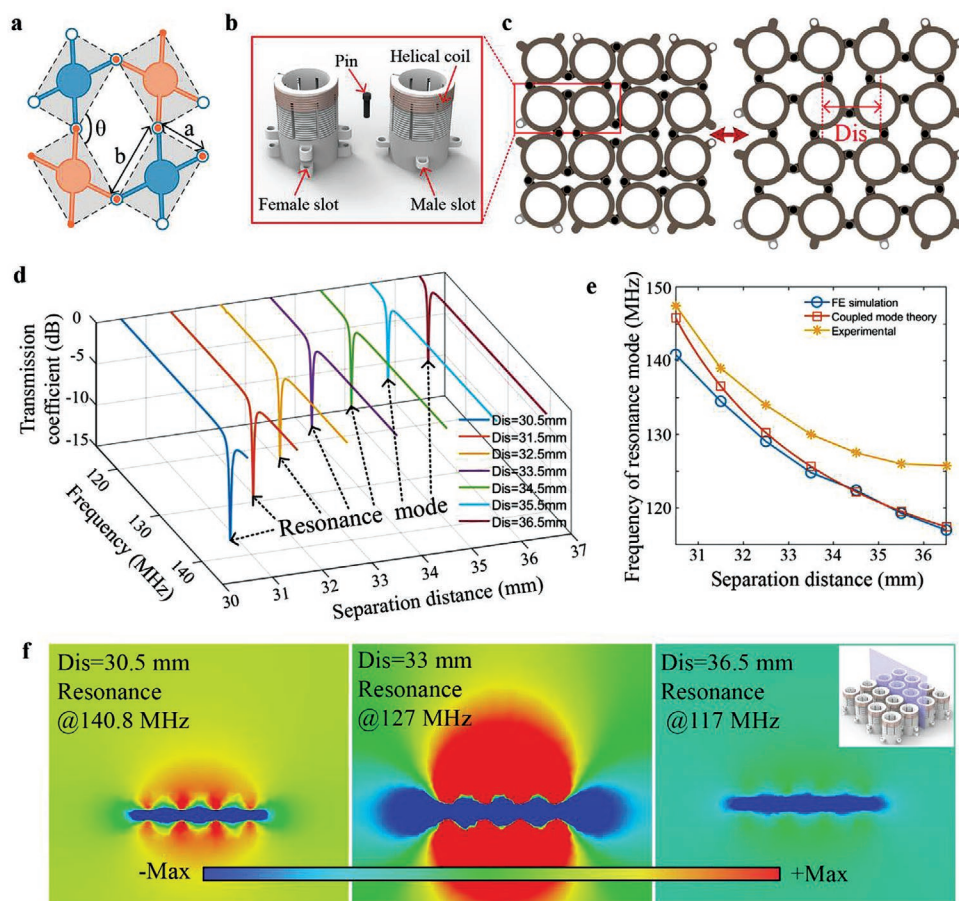


**Figure 1.** Design and electromagnetic properties analysis of the 2D tunable metamaterial. a) Schematic of “rotating rigid polygon” type of auxetic structure. b) Illustration of structural deformation ( $Dis$  is defined as the separation distance between the centers of neighboring unit cells). c) Magnified schematic of the unit cells of the 2D planar tunable metamaterial. d) Transmission coefficient as a function of frequency and separation distance  $Dis$ . e) Tunability of the resonance mode frequency as a function of separation distance  $Dis$ . f) Magnetic field strength @127 MHz along the axial direction distributed along the metamaterial cross-section (depicted as the blue plane in the inset) for varied separation distances:  $Dis = 30.5$  mm,  $Dis = 33$  mm, and  $Dis = 36.5$  mm.

herein for subsequent experimental validation and fix the space between two turns and the number of turns of the helical coils at 1.25 and 7.25 mm, respectively. First, numerical simulation using CST Microwave Studio was performed, with a series of frequency responses of the metamaterial at different separation distances plotted in Figure 1d, in which resonant modes are identified as dips on the plotted curves. The resonance frequencies of this 2D tunable metamaterial were extracted from simulation results as a function of separation distance  $Dis$ . Moreover, theoretical analyses based on the coupled mode theory were also performed for the metamaterial. The resonant mode of the metamaterial as a function of separation distance may be derived by solving the following equation system<sup>[27]</sup>

$$\frac{da_n(t)}{dt} = -(j\omega_0 + \Gamma_n)a_n(t) + j\sum_{k=1}^{m, k \neq n} K_{kn}a_k(t), \quad n = 1, \dots, m \quad (2)$$

in which  $a_k$  refers to the mode amplitude of the  $k_{th}$  element in metamaterial,  $\omega_0$  represents the resonant angular frequency of a single helix,  $\Gamma_n$  is the intrinsic decay introduced by the material and radiation losses,  $K_{kn}$  is the coupling factor among unit

cells and  $m$  is the total number of unit cells in the metamaterial. Details of the calculations may be found in Section S3 of the Supporting Information. Finally, in order to validate the simulation and calculation results, we experimentally analyzed the resonance frequency as a function of metamaterial separation distance. Simulation results, theoretical calculations, and experimental results are depicted in Figure 1e, demonstrating that an  $\approx 20$  MHz frequency shift of the resonance mode may be achieved across the full range of mechanical deformation. The coincident frequency shift between the theoretical calculation and experimental results serves to validate the theoretical analysis based on the coupled mode theory. The differences present in Figure 1e between the simulation and experimental results may be due to the modeling of the scaffold, which may result in discrepancies between the approximation in simulations and the actual laboratory experiments. The frequency match between the metamaterial and the MRI system is paramount to optimize the enhancement of the RF magnetic field strength and, ultimately, the SNR of the resultant MRI images. The impact of frequency matching on the RF field enhancement ratio is investigated to demonstrate the necessity of the

tunability of the metamaterial. Based on simulation results, the magnetic field distribution, assuming operation at 3 T MRI (127 MHz), as a function of metamaterial array deformation and resultant variations in array resonance frequency, is illustrated in Figure 1f. The leftward color map in Figure 1f depicts the magnetic field distribution on the cutting plane (indicated in the inset figure) when the separation distance  $Dis$  between neighboring unit cells in metamaterial is adjusted to 30.5 mm and the corresponding resonance frequency of metamaterial is 140.8 MHz. The middle color map in Figure 1f illustrates the magnetic field distribution when  $Dis$  is tuned to 33 mm, which yields an optimized resonance frequency of 127 MHz of the metamaterial array, matching the operating frequency of MRI system. The rightward color map demonstrates the magnetic field distribution when  $Dis$  is increased to 36.5 mm, resulting in a metamaterial resonance frequency of 117 MHz. The dramatic weakening of the magnetic field distribution in both of the off-resonance scenarios supports the conclusion that frequency matching between the metamaterial array and the MRI system is fundamental to optimizing the field enhancement effect for the metamaterial and, ultimately, its performance in MRI. Given the clear need for frequency matching, we further conclude that metamaterial tunability is paramount to its eventual successful clinical adoption in MRI, given the known resonance shifts that may commonly be imposed on the metamaterial due to differences in patient body or phantom composition. See Section S4 of the Supporting Information for further details regarding the resonance shift due to different phantom compositions. The experimental results plotted in Figure S4 (Supporting Information) demonstrates the resonance frequency tuning capacity of the 2D metamaterial while considering real-world clinical MRI applications.

## 2.2. 3D Tunable Metamaterials

Turning our attention to 3D metamaterials, notable is the fact that 3D deployable auxetics assembled using angulated scissor elements have been developed and reported with respect to their applications in structural engineering and architecture.<sup>[28]</sup> A well-known application of 3D deployable auxetics is the Hoberman sphere,<sup>[29–31]</sup> a popular educational toy. A Hoberman sphere is an isokinetic structure that resembles a geodesic dome, which is capable of contraction and expansion via a scissor-like action of its joints, all while maintaining its global, spherical shape. Inspired by the geometric features and deformation mechanisms of the Hoberman sphere, we developed a tunable 3D metamaterial based on the concept of an angulated scissor hinge system. More specifically, herein, we focus on the design of a hemispherical tunable metamaterial, considering its application to brain imaging and conformation to the human head. In order to distribute the unit cells of metamaterial uniformly on the surface of the hemisphere, a polyhedron tessellated with 75 isosceles triangles was modeled to form an approximately hemispherical surface, with 46 cylinders representing unit cells allocated on the vertices of these triangles. It should be noted that the lines connecting the center points of the polyhedrons  $O$  to the vertices of these isosceles triangles have the same length, and the center of the

polyhedron is regarded as the deployable center (modeling process is detailed in Section S2 and Figure S2 of the Supporting Information). Furthermore, the rod lengths between neighboring vertices are not perfectly equal; the rigid rods could be decomposed into three distinct types with different lengths indicated by the yellow, red, and blue colors, respectively, as shown in Figure 2a. Next, angulated scissor linkages were designed to replace these rigid rods, as shown in Figure 2b, thus achieving the auxetic structure of the 3D tunable metamaterial. The dimensions of the angulated scissor linkages may be expressed by

$$\beta_{1,2,3} = \pi - \frac{\alpha_{1,2,3}}{2} \quad (3)$$

$$m_{2,3} = m_1 \frac{\sin(\alpha_{2,3}/2)}{\sin(\alpha_1/2)} \quad (4)$$

$$L_{a-1,2,3} = \frac{1}{2} [R \tan(\alpha_1/2) - m_1] \quad (5)$$

$$L_{b-1,2,3} = \sqrt{L_{a-1,2,3}^2 + \left( R - \frac{m_{1,2,3}}{\tan(\alpha_{1,2,3}/2)} \right)^2} \sin \left( \frac{\alpha_{1,2,3}}{2} - \arctan \left( \frac{L_{a-1,2,3}}{R - \frac{m_{1,2,3}}{\tan(\alpha_{1,2,3}/2)}} \right) \right) \quad (6)$$

in which  $\alpha_1$ ,  $\alpha_2$ , and  $\alpha_3$  represent the central angles formed by connecting the central point  $O$  of the polyhedron to two ends of the yellow, red, and blue rods, respectively, and  $\beta_1$ ,  $\beta_2$ , and  $\beta_3$  represent the angles of the corresponding angulated scissor linkages.  $m_1$ ,  $m_2$ , and  $m_3$  are the offset lengths reserved for the connection between hubs and linkages.  $L_{a-1}$  and  $L_{b-1}$ ,  $L_{a-2}$  and  $L_{b-2}$ , and  $L_{a-3}$  and  $L_{b-3}$  represent the lengths of the angulated scissor linkages replacing the yellow, red, and blue rods, respectively, as shown in Figure 2a. Details regarding design of the linkages may be found in Section S2 and Figure S3 of the Supporting Information. Note, all relevant dimensions are illustrated in Figure 2b. In addition to the angulated scissor linkages, hubs with embedded slots were designed to serve as connection joints to support these angulated scissor linkages. Furthermore and importantly, the hubs also play the role of scaffolding for mounting the helical metallic coils of the metamaterial's unit cells. Following this geometric design process, all angulated scissor linkages and hubs were 3D printed and assembled into a deployable dome structure by connecting all the hubs through the angulated scissor linkages. Figure 2c is an illustrative example of the manner in which neighboring unit cells and their interconnecting angulated linkages were assembled and also demonstrates the expansion and contraction process of a sample set of unit cells. Figure 2d represents a magnified illustration of the 3D tunable metamaterial, highlighting the assembly details. Figure 2e illustrates the entirety of the designed 3D deployable metamaterial, demonstrating its auxetic deformation. The fabrication results may be found in Section S1 and Figure S1 in the Supporting Information.



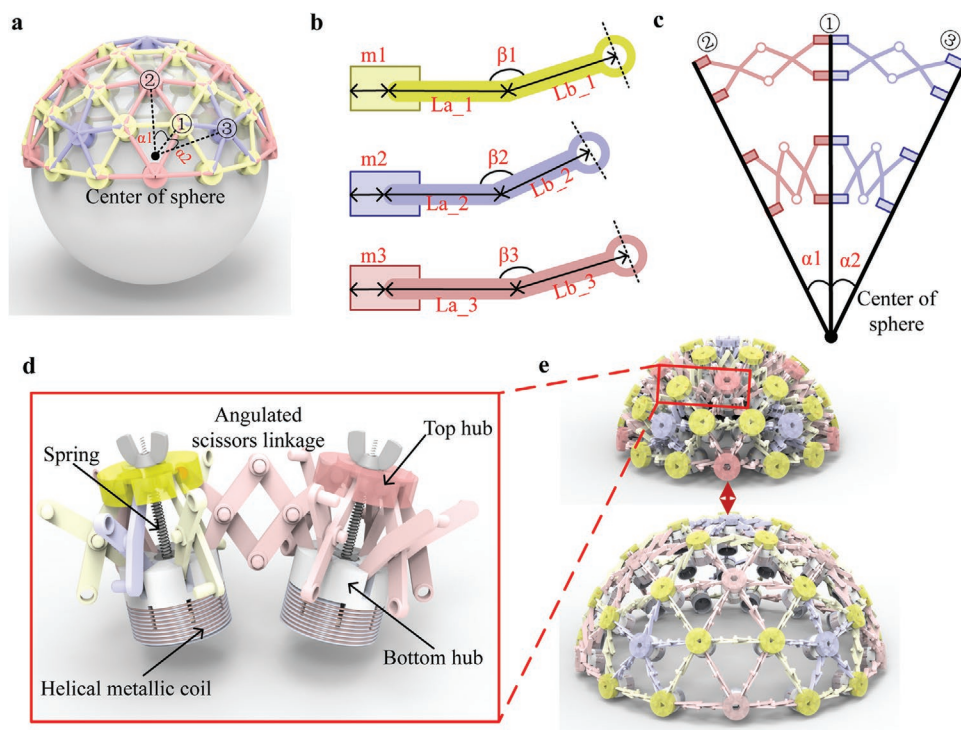


**Figure 2.** Design of the 3D tunable metamaterial. a) Modeling the 3D hemispherical metamaterial. b) Angulated scissor linkages designed to replace the corresponding rods of the same color shown in (a) (dimensions indicated for subsequent analyses). c) Illustration of the manner of assembling neighboring unit cells and interconnecting angulated linkages. d) Magnified conceptual image of discrete, interconnected unit cells of the 3D hemispherical, tunable metamaterial. e) Illustration of the deformation of the 3D metamaterial.

Similar to the 2D tunable metamaterial, numerical simulations, theoretical analysis, and experimental validations were performed to investigate the impact of mechanical deformation on the electromagnetic properties of the 3D deployable metamaterial. Notable is that only a partial hemispherical metamaterial composed of 16 unit cells was taken into consideration when analyzing the electromagnetic properties due simply to computational limitations. The simulated frequency response as a function of the radius of the 3D metamaterial is plotted in **Figure 3a**, in which the resonant modes are identified as dips on these plotted curves. The resonance mode frequencies as a function of spherical radius  $R_{ad}$  are extracted from simulation results and depicted in **Figure 3b**, demonstrating that an  $\approx 20$  MHz frequency shift of the resonance mode could be achieved from the auxetic deformation. For comparison, theoretical calculations based on the coupled mode theory and experimental analyses are also performed to derive the resonance frequency as a function of the radius of the metamaterial  $R_{ad}$  and plotted in **Figure 3b**. Further details regarding the resonance shift due to different phantom compositions for this spherical metamaterial are discussed in Section S4 of the Supporting Information. **Figure S5** (Supporting Information) demonstrates the tuning capacity of the 3D metamaterial while considering real-world clinical MRI applications. In addition, the enhancement of the RF field strength due to the metamaterial was also simulated to investigate the impact of frequency

matching between the metamaterial and the MRI system. A group of color maps of magnetic field distribution are depicted in **Figure 3c**, with the influence of variations in metamaterial radius and its consequent effect on metamaterial resonance frequency illustrated. As in the case of the 2D, planar version, frequency mismatch is demonstrated to strongly influence field enhancement to a degree such that the field is actually decreased in the scenario in which the metamaterials' resonance frequency is lower than the working frequency of the MRI.

### 3. Experimental MRI Validation

#### 3.1. MRI Validation for 2D Tunable Metamaterials

In order to evaluate the performance of the tunable metamaterials, experimental validation of the SNR enhancement in the presence of the metamaterials was performed using phantoms in a 3 T clinical MRI system. In order to calculate the SNR values for the MRI images, the two-image method was employed.<sup>[32]</sup> In the case of the 2D tunable metamaterial, a bottle-shaped phantom filled with mineral oil was employed for imaging. The metamaterial array was placed along the undersurface of the phantom, the bottom surface of which was  $\approx 10$  mm from the top surface of the metamaterial; the experimental setup is shown in **Figure 4a**. We initially imaged the phantom in the absence of the metamaterial,

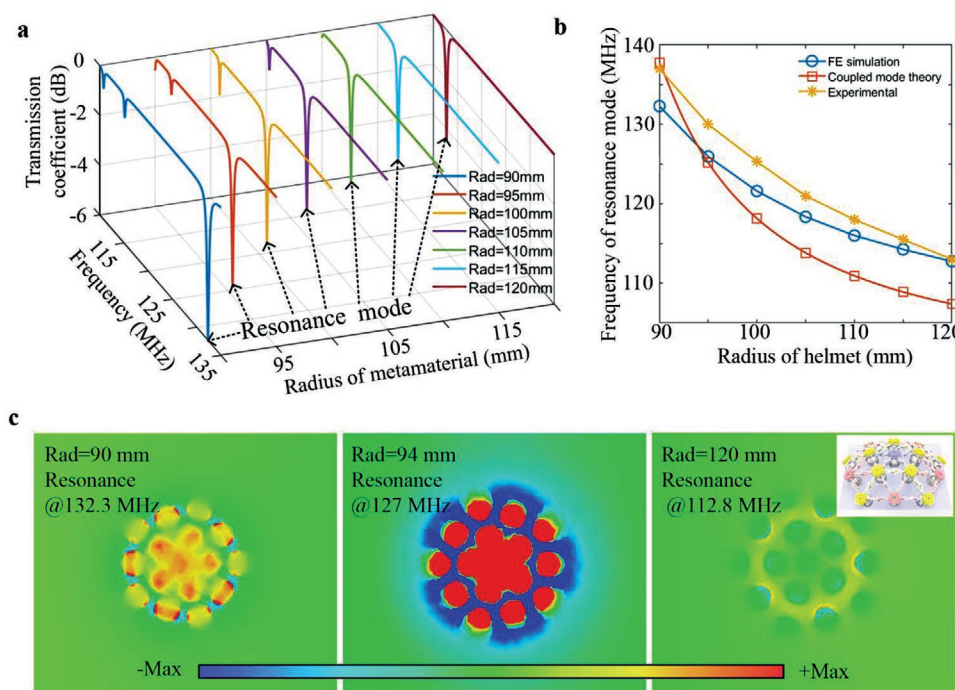


**Figure 3.** Electromagnetic properties analysis of the 3D tunable metamaterial. a) Transmission coefficient as a function of the frequency and radius of the 3D tunable metamaterial  $Rad$ . b) Tunability of the resonance mode frequency as a function of  $Rad$ . c) Magnetic field strength @127 MHz along the axial direction distributed along the metamaterial cross-section (depicted as the inset, upper right) for various radii:  $Rad = 90$  mm,  $Rad = 94$  mm, and  $Rad = 120$  mm, left to right, respectively.

which served as a reference standard and is depicted in Figure 4b. Next, we adjusted the separation distance  $Dis$  in the metamaterial to its maximal value, thereby leading to a resonance frequency lower than 127 MHz. Under this frequency-mismatched state, the phantom was scanned in the presence of metamaterial, with the resultant image depicted in Figure 4c. Compared with the reference acquired in the absence of the metamaterial, there was an area of relative signal loss in the image, without any obvious improvement in the image quality. Subsequently, the resonance frequency of the 2D metamaterial was tuned to 127 MHz by decreasing the separation distance  $Dis$  in the metamaterial, thereby realizing the optimal condition of a resonance match between the metamaterial and the MRI system. Importantly, during the tuning process, the phantom was in proximity to the metamaterial in the identical orientation (Figure 4a) as the subsequent MRI validation in order to compensate for detuning effects related to the presence of the phantom. The image acquired under the optimized resonance state of the phantom is depicted in Figure 4d, demonstrating marked improvement in overall SNR, up to 4.5-fold when compared to the acquisition in the absence of the metamaterial. Details of the analysis and calculations related to SNR improvement for the 2D metamaterial may be found in Section S5 of the Supporting Information. Finally, we continued to decrease the separation distance  $Dis$  in the metamaterial to yield a resonance frequency of the metamaterial in excess of the 127 MHz operating frequency of the MRI. The image acquired under these conditions is shown in Figure 4e, demonstrating no significant gains in SNR.

### 3.2. MRI Validation for the 3D Tunable Metamaterial

Subsequently, a similar experimental approach was performed with the 3D metamaterials. In order to maintain consistency with the numerical simulation and theoretical analysis, a 3D metamaterial composed of 16 unit cells was employed in the MRI experiments. A spherical phantom filled with mineral oil was prepared for experimental validation of the MRI SNR enhancement; the experimental setup is illustrated in Figure 5a. Figure 5b presents the captured image in the absence of the metamaterial, serving as a reference standard. Ranging from an expanded to a contracted state of the 3D deployable metamaterial, the resonance frequency was tuned to lower than 127 MHz, equal to 127 MHz and higher than 127 MHz, respectively, similar to the experiments performed using the 2D metamaterial version above. Under these three corresponding resonance frequencies, the spherical phantom was imaged using MRI, with the captured images depicted in Figure 5c,d,e. As in the 2D metamaterial, the matched-resonance state resulted in a maximally increased SNR in excess of 2.5-fold when compared to the reference state in the absence of the metamaterial (the analysis and reasoning for the improved SNR is explained in further detail in Section S5 of the Supporting Information). Also notable is the similarity in pattern between the RF field simulations in Figure 3c and the MRI images acquired using the 3D metamaterial in Figure 5d, further supporting the direct relevance between the degree of RF field enhancement and eventual SNR during image acquisition. Again, the fundamental importance of resonance matching is clearly illustrated in the case of the 3D metamaterial, as in the 2D version above, further

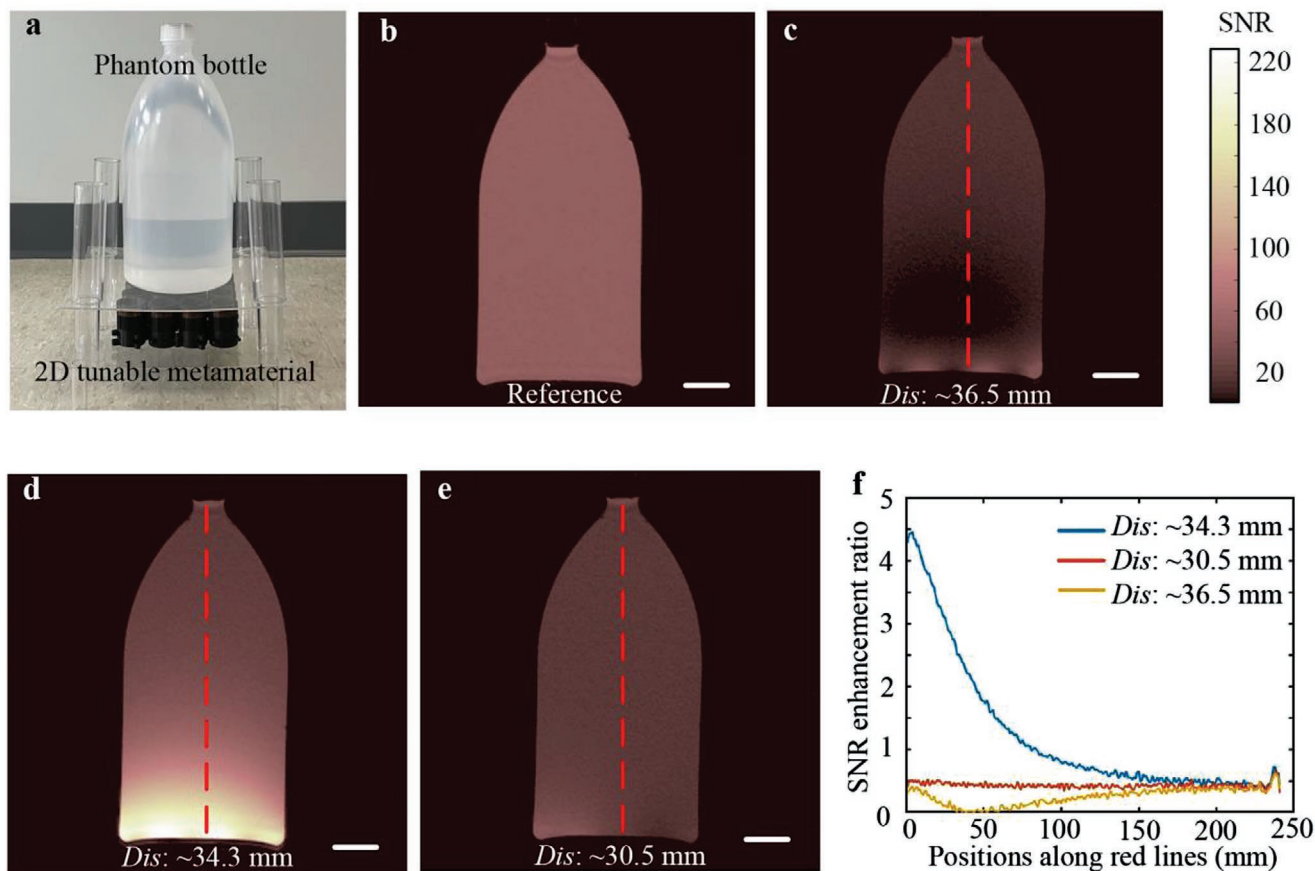


**Figure 4.** 3 T MRI imaging of mineral bottle phantom. Gradient echo imaging employed. a) Photo of the experimental setup for the 2D tunable metamaterial. b) Image acquired by body coil in absence of metamaterial, serving as a reference. c) Image acquired in presence of a metamaterial with a lower resonance frequency than MRI system. d) Image captured in presence of metamaterial exhibiting a frequency match with MRI system. e) Image captured in presence of metamaterial with a higher resonance frequency than MRI system. f) Comparison of the SNR enhancement ratio for the three metamaterials of differing resonance frequency along the red dashed lines in (c), (d), and (e). Scale bars in (b), (c), (d), and (e) are 3 cm.

supporting the need for the capacity for tunability in applying metamaterial technology in MRI.

Finally, in addition to the experimental MRI validation using the mineral oil phantoms, we also employed *ex vivo* samples of porcine brain in order to preliminarily demonstrate the performance of the 3D metamaterial in biomedically relevant imaging. The test sample was made of a hollow hemispherical structure with a wall thickness of 75 mm and a diameter of 176 mm, which was fully filled with porcine brain samples in order to mimic brain imaging, as shown in **Figure 6a**. 10 slices (images) were acquired in the planes parallel to *xy*-plane; the slice thickness and slice increment were 5 and 4.5 mm, respectively. During these experiments, we employed turbo field echo (TFE) imaging, a gradient echo pulse sequence with data acquisition after an initial  $180^\circ$  preparatory pulse for contrast enhancement. The scan images from slice #1 to #10 are depicted in **Figure 6b** with and without the 3D metamaterial. Noise of these images are normalized to the same level. When compared to images acquired in the absence of the metamaterial array, images with enhanced signal strength were achieved in the presence of the metamaterial. These acquired images for porcine brain provide a preliminary demonstration of that potential.

## 4. Conclusion

The design, fabrication, and characterization of auxetics-enabled 2D planar and 3D hemispherical tunable magnetic metamaterials composed of arrays of metallic helices, which serve to enhance RF magnetic fields and increase SNR in their application to MRI, is reported. Following the introduction of the concept of tuning the resonance mode frequency by varying the density of meta-atoms through appropriately designed 2D and 3D auxetic structures, the observed resonance shift is addressed using the coupled mode theory, simulation, and experimental analyses, deriving the influence of the metamaterials' resonance modes on their RF field enhancement effects. Finally, MRI validations were undertaken in two clinically relevant scenarios using planar and 3D types of auxetic metamaterials. There exist a large number of possible implementations of tunable metamaterials inspired by the concepts of auxetic structures due to their inherent design flexibility. For example, the tuning mechanism presented herein may be further developed and applied to yield arbitrarily shaped 3D tunable metamaterials, which could be employed for imaging less regular portions of the human anatomy (ankle, knee, shoulder, breasts, and neck, as examples) in a conformal fashion. Furthermore,



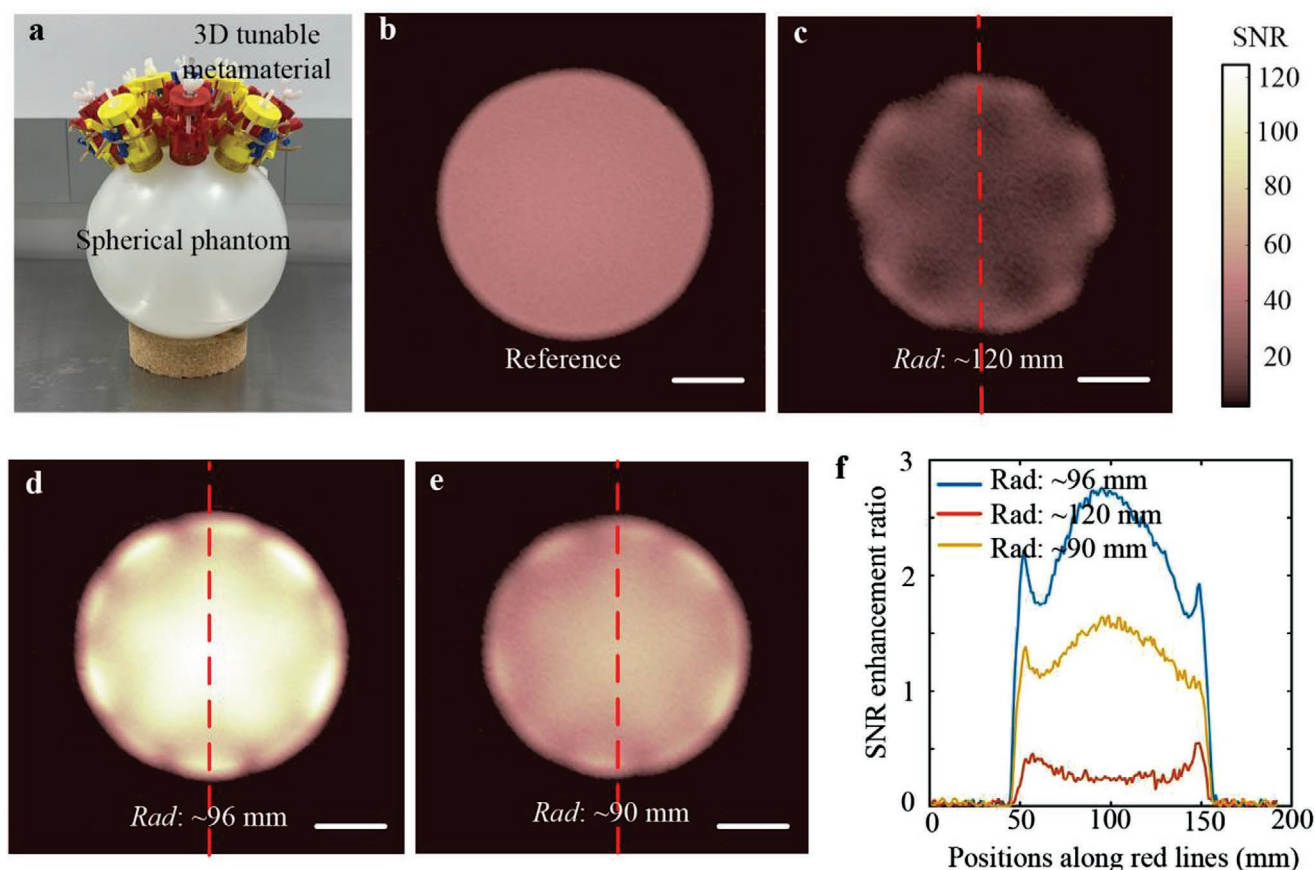


**Figure 5.** 3 T MRI imaging of mineral spherical phantom. Gradient echo imaging employed. a) Experimental setup for the 3D tunable metamaterial. b) Image acquired using body coil in absence of metamaterial using spherical phantom as a reference. c) Image acquired in presence of metamaterial with a lower resonance frequency than MRI system. d) Image captured in presence of metamaterial exhibiting a frequency match with the MRI system. e) Image captured in presence of a metamaterial with a higher resonance frequency than MRI system. f) Comparison of the SNR enhancement ratio for the three metamaterials of differing resonance frequency along the red dashed lines in (c), (d), and (e). Scale bars in (b), (c), (d), and (e) are 3 cm.

beyond the application to MRI, auxetic behavior is theoretically scale-independent, with the same deformation mechanisms operating at the macro-, micro-, and nanolevels. Therefore, this tuning mechanism offers a promising pathway for the future development of application-oriented electromagnetic devices operating across a range of designated frequencies.

## 5. Experimental Section

**Fabrication of the Metamaterial:** In fabricating the tunable metamaterials, copper wire with a radius of 0.28 mm was wound into the scaffolding grooves to form the metallic resonator composing each unit cell of the metamaterial array. All the scaffolds were fabricated by 3D printing and subsequently assembled into 2D/3D metamaterial arrays; the fabrication results are illustrated in Figure S1 (Supporting Information).

**Characterization of Metamaterial Resonance Frequency:** A network analyzer (E5071C, Keysight Inc.) was employed with an inductive loop to excite the magnetic resonance of the 2D/3D metamaterials and measure the reflection spectra. In the reflection spectra, the dips correspond to the resonance mode of the metamaterials.

**MRI Validation:** The performance of the 2D and 3D metamaterials with respect to their degrees of MRI SNR improvement using a 3 T MRI system (Philips Healthcare) was validated. The metamaterial was

placed in the bore of the MRI system and the body coil was employed for both RF transmission and reception, as shown in Figures 4a and 5a. A bottle-shaped and a spherical phantoms composed of mineral oil were employed for the MRI imaging experiments. Gradient echo (GRE) imaging was employed with echo time (TE) and repetition time (TR) of 4.6 and 100 ms, respectively. During the imaging sequence of this validation, GRE imaging was first performed to capture an image of the phantom, followed by capturing a noise image by shutting down the transmission RF coil. The SNR in the region of interest was calculated as the ratio between the mean value of magnitude image and the standard deviation of the noise image, as shown in Figure S9 (Supporting Information). For the 2D metamaterial, the matrix size was  $288 \times 288 \text{ mm}^2$ , the pixel size was  $1 \times 1 \text{ mm}^2$ , and the slice thickness was 5 mm. A flip angle of  $90^\circ$  was employed in the reference (without metamaterial) imaging experiments. In the 2D metamaterial imaging experiments, the energy of the excitation RF field was reduced by a factor of 6 (flip angle =  $15^\circ$ ) in order to ensure that the flip angle along the bottom of phantom, in proximity to the transmission RF-magnifying metamaterial, did not exceed  $90^\circ$ . For the 3D metamaterial, the matrix size was  $192 \times 192 \text{ mm}^2$ , the pixel size was  $1 \times 1 \text{ mm}^2$ , and the slice thickness was 5 mm. A flip angle of  $90^\circ$  was employed in the reference (without metamaterial) imaging experiments. In the 3D metamaterial imaging experiments, the energy of the excitation RF field was reduced by a factor of 3 (flip angle =  $30^\circ$ ) in order to ensure that the flip angle along the bottom of phantom, in proximity to the transmission RF-magnifying metamaterial, did not exceed  $90^\circ$ .

**Numerical Simulation:** The simulation of the metamaterial was performed using the frequency domain method with CST Microwave



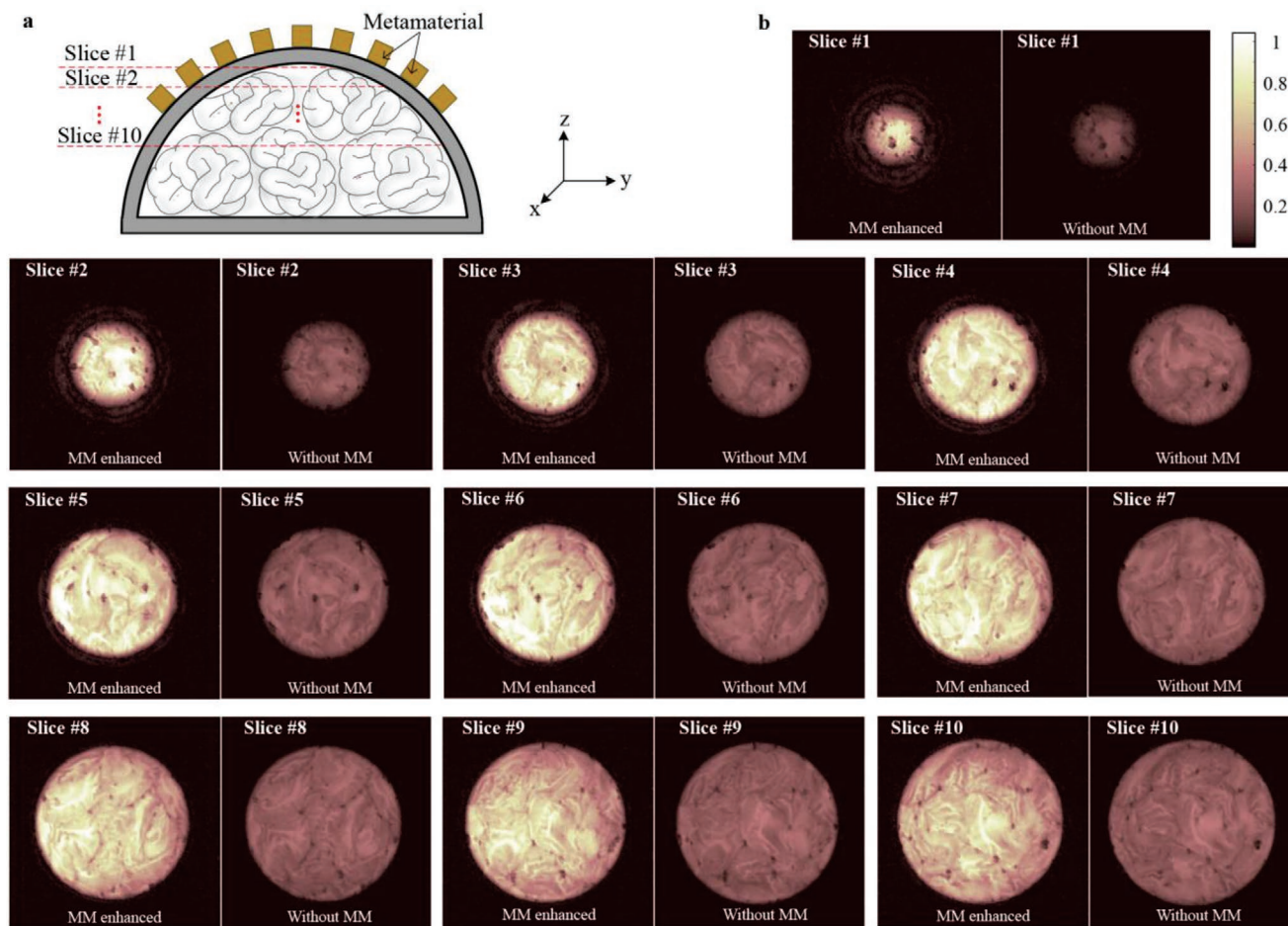


**Figure 6.** MRI scan of ex vivo porcine brain. a) The conceptual drawing of experimental setup for the 3D tunable metamaterial. b) Comparisons between images with and without metamaterial enhanced acquired on the cutting planes, as shown in (a).

Studio software. In the simulation model, the dimensions of the metamaterial were the same as the fabricated sample described above. The scaffolding of the metamaterial unit cell was modeled as a dielectric material with permittivity of 2.6 and the copper wire was considered to be a metal with conductivity of  $5.96 \times 10^7 \text{ S m}^{-1}$ .

## Supporting Information

Supporting Information is available from the Wiley Online Library or from the author.

## Acknowledgements

K.W. and X.Z. contributed equally to this work. This research was supported by the National Institute of Health (NIH) of Biomedical Imaging and Bioengineering Grant No. 1R21EB024673. The authors are grateful to Dr. Yansong Zhao and Samantha Averitt for their experimental assistance during the MRI testing. The authors thank Boston University Photonics Center for technical support. The porcine brain samples used in this work were obtained from a local butcher shop

## Conflict of Interest

The authors have filed a patent application on the work described herein, application No.: 16/002,458 and 16/443,126. Applicant: Trustees of

Boston University. Inventors: Xin Zhang, Stephan Anderson, Guangwu Duan, and Xiaoguang Zhao. Status: Active.

## Data Availability Statement

The data that support the findings of this study are available from the corresponding author upon reasonable request.

## Keywords

auxetics, magnetic coupling, magnetic resonance imaging, signal-to-noise ratio, tunable metamaterials

Received: November 8, 2021  
Published online: December 19, 2021

- [1] X. Zhang, Z. Liu, *Nat. Mater.* **2008**, *7*, 435.
- [2] T. Taubner, D. Korobkin, Y. Urzhumov, G. Shvets, R. Hillenbrand, *Science* **2006**, *313*, 1595.
- [3] I. Landy, S. Sajuyigbe, J. J. Mock, D. R. Smith, W. J. Padilla, *Phys. Rev. Lett.* **2008**, *100*, 207402.
- [4] X. Zhao, J. Zhang, K. Fan, G. Duan, G. D. Metcalfe, M. Wraback, X. Zhang, R. D. Averitt, *Photonics Res.* **2016**, *4*, A16.

- [5] D. Schurig, J. J. Mock, B. J. Justice, S. A. Cummer, J. B. Pendry, A. F. Starr, D. R. Smith, *Science* **2006**, *314*, 977.
- [6] W. Cai, U. K. Chettiar, A. V. Kildishev, V. M. Shalae, *Nat. Photonics* **2007**, *1*, 224.
- [7] Y. Dong, T. Itoh, *Proc. IEEE* **2012**, *100*, 2271.
- [8] A. P. Slobozhanyuk, A. N. Poddubny, A. J. E. Raaijmakers, C. A. T. van den Berg, A. V. Kozachenko, I. A. Dubrovina, I. V. Melchakova, Y. S. Kivshar, P. A. Belov, *Adv. Mater.* **2016**, *28*, 1832.
- [9] G. Duan, X. Zhao, S. W. Anderson, X. Zhang, *Commun. Phys.* **2019**, *2*, 35.
- [10] I. V. Shadrivov, P. V. Kapitanova, S. I. Maslovski, Y. S. Kivshar, *Phys. Rev. Lett.* **2012**, *109*, 083902.
- [11] W. Lewandowski, M. Fruhnert, J. Mieczkowski, C. Rockstuhl, E. Górecka, *Nat. Commun.* **2015**, *6*, 6590.
- [12] H. T. Chen, W. J. Padilla, J. M. O. Zide, A. C. Gossard, A. J. Taylor, R. D. Averitt, *Nature* **2006**, *444*, 597.
- [13] S. Lee, S. Kim, T.-T. Kim, Y. Kim, M. Choi, S. H. Lee, J.-Y. Kim, B. Min, *Adv. Mater.* **2012**, *24*, 3491.
- [14] X. Zhao, J. Schalch, J. Zhang, H. R. Seren, G. Duan, R. D. Averitt, X. Zhang, *Optica* **2018**, *5*, 303.
- [15] D. A. Powell, M. Lapine, M. V. Gorkunov, I. V. Shadrivov, Y. S. Kivshar, *Phys. Rev. B* **2010**, *82*, 155128.
- [16] R. Singh, C. Rockstuhl, W. Zhang, *Appl. Phys. Lett.* **2010**, *97*, 241108.
- [17] T. C. Lim, *Auxetic Materials and Structures*, Springer, Berlin, Germany **2015**.
- [18] H. M. A. Kolken, A. A. Zadpoor, *RSC Adv.* **2017**, *7*, 5111.
- [19] X. Ren, R. Das, P. Tran, T. D. Ngo, Y. M. Xie, *Smart Mater. Struct.* **2018**, *27*, 023001.
- [20] W. Yang, Z.-M. Li, W. Shi, B.-H. Xie, M.-B. Yang, *J. Mater. Sci.* **2004**, *39*, 3269.
- [21] Z. Wang, H. Hu, *Text. Res. J.* **2014**, *84*, 1600.
- [22] A. Alderson, J. Rasburn, S. Ameer-Beg, P. G. Mullarkey, W. Perrie, K. E. Evans, *Ind. Eng. Chem. Res.* **2000**, *39*, 654.
- [23] R. Gatt, L. Mizzi, J. I. Azzopardi, K. M. Azzopardi, D. Attard, A. Casha, J. Briffa, J. N. Grima, *Sci. Rep.* **2015**, *5*, 8395.
- [24] W. A. Smith, *Proc. IEEE Ultrasonics Symp.* **1991**, *1*, 661.
- [25] Y. Ma, F. Scarpa, D. Zhang, B. Zhu, L. Chen, J. Hong, *Smart Mater. Struct.* **2013**, *22*, 084012.
- [26] J. N. Grima, K. E. Evans, *J. Mater. Sci. Lett.* **2000**, *19*, 1563.
- [27] H. A. Haus, *Waves and Fields in Optoelectronics*, Prentice-Hall, Inc., Englewood Cliffs, NJ, USA **1984**.
- [28] N. Friedman, G. Farkas, A. Ibrahimbegovic, *Pollack Period.* **2011**, *6*, 85.
- [29] C. Hoberman US 4942700, 1990.
- [30] C. Hoberman US 5024031, 1991.
- [31] X. Sun, Y. Yao, R. Li, *Front. Mech. Eng.* **2020**, *15*, 89.
- [32] F. L. Goerner, G. D. Clarke, *Med. Phys.* **2011**, *38*, 5049.